

LETTER TO THE EDITOR

Herschel PACS and SPIRE imaging of CW Leo [★]

D. Ladjal¹, M.J. Barlow², M.A.T. Groenewegen³, T. Ueta⁴, J.A.D.L. Blommaert¹, M. Cohen⁵, L. Decin^{1,6}, W. De Meester¹, K. Exter¹, W. K. Gear⁷, H. L. Gomez⁷, P. C. Hargrave⁷, R. Huygen¹, R. J. Ivison⁸, C. Jean¹, F. Kerschbaum⁹, S. J. Leeks¹⁰, T. L. Lim¹⁰, G. Olofsson¹¹, E. Polehampton^{10,12}, T. Posch⁹, S. Regibo¹, P. Royer¹, B. Sibthorpe⁸, B. M. Swinyard¹⁰, B. Vandenbussche¹, C. Waelkens¹, and R. Wesson²

(Affiliations can be found after the references)

Received:2010 / accepted:2010

ABSTRACT

Herschel PACS and SPIRE images have been obtained over a 30'×30' area around the well-known carbon star CW Leo (IRC +10 216). An extended structure is found in an incomplete arc of ~22' diameter, which is cospatial with the termination shock due to interaction with the interstellar medium (ISM) as defined by Sahai & Chronopoulos from ultraviolet GALEX images. Fluxes are derived in the 70, 160, 250, 350, and 550 μm bands in the region where the interaction with the ISM takes place, and this can be fitted with a modified black body with a temperature of 25±3 K. Using the published proper motion and radial velocity for the star, we derive a heliocentric space motion of 25.1 km s⁻¹. Using the PACS and SPIRE data and the analytical formula of the bow shock structure, we infer a de-projected standoff distance of the bow shock of $R_0 = (8.0 \pm 0.3) \times 10^{17}$ cm. We also derive a relative velocity of the star with respect to the ISM of $(106.6 \pm 8.7) / \sqrt{n_{\text{ISM}}}$ km s⁻¹, where n_{ISM} is the number density of the local ISM.

Key words. circumstellar matter – infrared:stars – stars: AGB and post-AGB – stars:carbon – stars: mass loss – stars: individual: CW Leo

1. Introduction

Ever since the discovery paper by Becklin et al. (1969), the object IRC +10 216 (= AFGL 1381 = CW Leo) has spurred much interest. We now know that it is a carbon star in an advanced stage of stellar evolution on the asymptotic giant branch (AGB), pulsating and surrounded by an optically thick dust shell and large molecular circumstellar envelope (CSE). One aspect of study has been to constrain the properties of the CSE by answering questions such as what is the mass-loss rate and how has it changed with time, what kind of chemistry takes place, and what is the geometry and structure of the CSE?

The deep optical images taken by Mauron & Huggins (1999, 2000), Mauron et al. (2003), and Leão et al. (2006) show that the dusty envelope is not smooth but consists of a series of arcs or incomplete shells. The average angular separation between the dust arcs suggests a timescale for the change in mass-loss rate of the order of 200–800 yr. The lack of kinematic information on the dust arcs precludes any firm conclusion about the true three-dimensional structure of the arcs or shells.

From large-scale mapping at a relatively low angular resolution of the CO J=1-0 emission, Fong et al. (2003) discovered a series of large molecular arcs or shells at radii of ~100'' in the outer envelope. They attribute these multiple shells as “being the reverberations of a single Thermal Pulse erupting over 6000 yr ago.” The timescale inferred from the spacing between these arcs is about 200–1000 yr.

In the present paper, we discuss our new results on the outer shell of CW Leo from observations with the *Herschel Space Observatory* (Pilbratt et al. 2010) and their connection to the

results from *GALaxy Evolution Explorer Space Observatory* (GALEX) by Sahai & Chronopoulos (2010, hereafter SC). For the present analysis, we adopted a distance of $d = 135$ pc and a mass-loss rate $\dot{M} = 2.2 \cdot 10^{-5} M_{\odot} \text{ yr}^{-1}$ (Groenewegen et al. 1998), a gas expansion velocity of $V_{\text{exp}} = 15.4$ km s⁻¹, a radial velocity $V_{\text{LSR}} = -25.5$ km s⁻¹ (Groenewegen et al. 2002), corresponding to $V_{\text{helio}} = -18.6$ km s⁻¹, and a proper motion (pm) $\mu_{\alpha} \cos \delta = +26 \pm 6$, $\mu_{\delta} = +4 \pm 6$ mas/yr (Menten et al. 2006).

2. Observations and data reduction

The observations were carried out using the Photo Array Camera & Spectrometer (PACS, Poglitsch et al. 2010) and the Spectral and Photometric Imaging REceiver (SPIRE, Griffin et al. 2010), and are part of the Science Demonstration Phase observations of the Mass-loss of Evolved StarS (MESS) guaranteed time key program (Groenewegen et al. 2010, in prep.), which is investigating the dust and gas chemistry and the properties of CSEs around a large sample of post-main-sequence objects.

For both instruments, the scan-map observing mode was used for a total sky coverage of 30'×30'. In this mode, the telescope is slewed at constant speed (20''/s for the PACS data, 30''/s for the SPIRE data) along parallel lines to cover the required area of the sky. For the PACS observations, two scan maps were taken with a scanning angle of 90° between the two to achieve the most homogeneous coverage. The observation identification numbers (obs.ID) for the two scans are: 1342186298 and 1342186299, with a total integration time of 8.35 hours. For the SPIRE observations, a single scan was taken (obs.ID 1342186293) with a total integration time of 1.35 hours. All observations were taken on 25 Oct. 2009.

The data reduction was performed using the *Herschel Interactive Processing Environment* (HIPE) version 2.3. We fol-

[★] Herschel is an ESA space observatory with science instruments provided by European-led Principal Investigator consortia and with important participation from NASA.

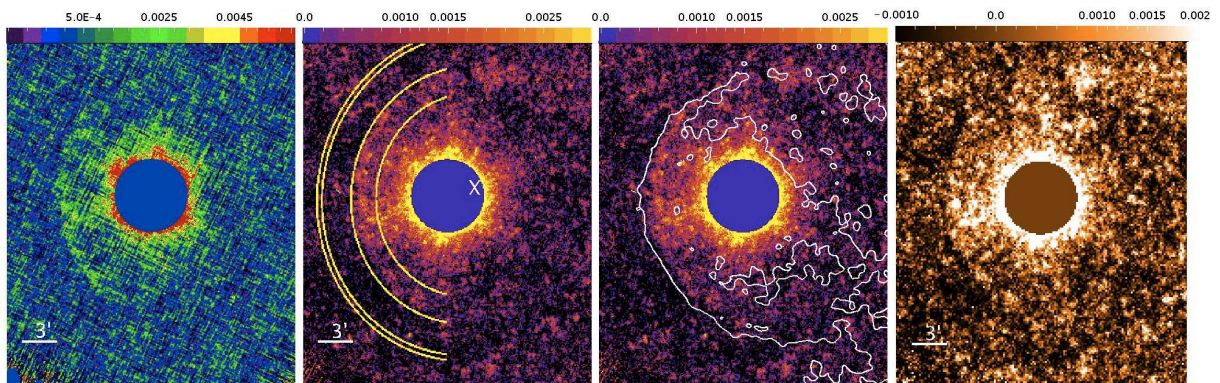


Fig. 1. Surface brightness maps in Jy/pixel. From left to right : PACS 160 μm image. SPIRE 250 μm image for which we overlotted the annuli segments between which we integrated the flux for the extended emission (inner annulus) and the sky (outer annulus). The white cross represents the center of the ellipse. SPIRE 250 μm image with overlotted in white the contour from the FUV map at $4.4 \times 10^{-5} \text{ mJy} \cdot \text{arcsec}^{-2}$ limit. SPIRE 350 μm image. The FOV for all images is $23' \times 27'$. Background sources were removed from all maps. North is up and east is to the left.

lowed the basic data reduction steps as described in the PACS data reduction guide v1.2 and the SPIRE data users manual v1.0 with the exception of the median filtering of the background. In the SPIRE pipeline, the entire scanline is used to calculate the median value. In the PACS pipeline, a running median filter is used with a certain “high pass filter width”. A value of 450 was adopted that leads to a spatial scale of filtering approximately equal to that used for the SPIRE data, and is of the order of $30'$. For both PACS and SPIRE, the central star was masked before applying the median filter. The mask was a circle around the central star that approximated a contour at 3σ of the background noise level.

Near-UV (NUV) and far-UV (FUV) GALEX data (Martin et al. 2005) were added to the analysis. The data were taken in 2008 and are centred around 1528\AA (FUV) and 2271\AA (NUV). We used the pipeline product retrieved from the GALEX archive.

3. Analysis

In the present paper, we do not comment on any structure close to the star previously detected in the optical and in CO. No similar structure is clearly visible in our data but a detailed analysis of the central structure requires a very detailed understanding and accurate subtraction of, or deconvolution with, the complicated PSF. This is beyond the scope of this paper.

The new result presented here is the extended emission in the form of an arc clearly seen at 160 μm , 250 μm , and 350 μm with a spatial scale as large as $22'$ (see Fig. 1). The arc is eastward of the central star with an almost circular curve. The central star is slightly to the east of the centre of the structure and the arc is slightly flattened in the easterly direction. It is interesting to note that this extended emission matches the position and the shape of the FUV extended emission (see Fig. 1). In the Herschel images, we do not see the patches of nebulosity seen in the western part of the FUV image (see Fig. 1 in SC).

The 1D intensity profile for each map (Fig. 2) was constructed by subtracting the total flux integrated within two successive apertures. To match the shape of the arc, elliptical aperture photometry was used. We only considered the area of the ellipse between 14° position angle (PA) and 167° PA (see Fig. 1) to match the spatial scale of the extended emission. The ellipses are centred on $\alpha = 146.955^\circ$ and $\delta = +13.28^\circ$ with a PA of -12° and a major-to-minor axis ratio taken to be 1.1. For the emission from the sky, the inner minor axis is $13.3'$ and the outer

minor axis is $13.8'$ (see Fig 1). The PACS fluxes were corrected following the numbers in the PACS Scan Map release note yielding an absolute flux calibration uncertainty of 10–20%. A similar correction was applied to the SPIRE fluxes following the correction factors given by Griffin et al. (2010) and Swinyard et al. (2010). The SPIRE absolute flux calibration uncertainty is $\sim 15\%$. The dust shell is detected at 160 μm , 250 μm , and 350 μm around $9.6'$ from the star for a maximal surface brightness of $0.067 \text{ mJy} \cdot \text{arcsec}^{-2}$ at 160 μm . There is an offset of $\sim 20''$ between the FUV intensity peak and the far-IR intensity peaks, which suggests that they have different origins.

Based on the location of the extended emission at 160 μm , the total flux in the arc was calculated within the segment of an elliptical annulus of $150''$ width, and inner minor axis of $8.5'$ between PA 14° and 167° (see Fig 1). The derived fluxes are listed in Table 1. The errors include the absolute calibration error and the error in the background estimation. We fitted the photometry of the extended emission with a function of the form $B_\nu \cdot \lambda^{-\beta}$, expected for a grain emissivity as $Q_{\text{abs}} \sim \lambda^{-\beta}$. The NUV and FUV data are plotted for reference, but these do not fit because the emission has a different physical origin (see below). The best fit solution infers a dust temperature of $25 \pm 3 \text{ K}$ and $\beta = 1.6 \pm 0.4$ (see Fig. 3). The value for β is in-between that expected for amorphous carbon (Rouleau & Martin 1991, $\beta = 1.1$) and astronomical silicates (Volk & Kwok 1988, $\beta = 2.0$), suggesting that the material in the bow shock is a mixture of C-rich material, lost by the star, and swept-up ISM material.

4. Discussion

4.1. Bow shock, thermal pulse, or both ?

The most widely accepted explanation of large detached shells is mass-loss variation (e.g., Olofsson et al. 1990, Zijlstra et al. 1992). AGB stars experience thermal pulses (TPs) during which intense mass loss ejections occur. A star can undergo several TPs, which would lead to the formation of concentric spherical detached shells (see Kerschbaum et al. 2010).

Another explanation of detached envelopes is the interaction between the AGB wind and the interstellar medium (ISM) (e.g. Young et al. 1993, Martin et al. 2007, Ueta et al. 2006). In this scenario, the AGB wind is slowed down as it sweeps up material from the ISM. The piled up material forms a density enhancement that continue to expand due to the internal pressure. Shocks

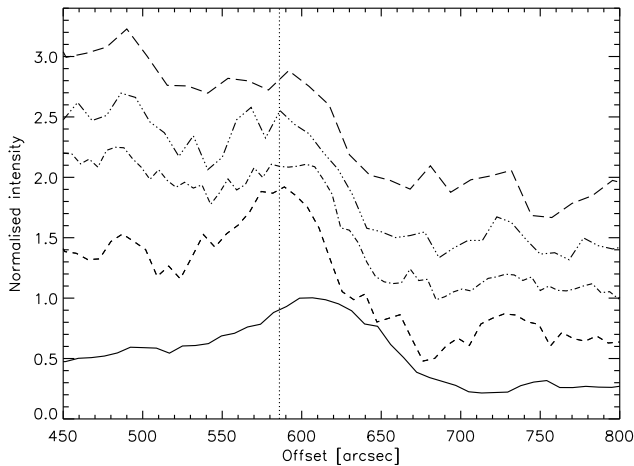


Fig. 2. Intensity profiles as a function of the offset along the minor axis of the ellipse increasing from west to east. The profile for each wavelength was normalised to the intensity at 558'' and shifted up for clarity. From bottom to top with normalisation factor in mJy/arcsec² and the vertical shift: FUV (0.065,0.0), 160 μm (0.063,0.8), 250 μm (0.023,1.1), 350 μm (0.008,1.4), 500 μm (0.004,1.8). The vertical dotted line indicates the position of the dust emission peak from the center of the ellipse.

can occur if the relative velocity of the AGB wind with respect to the ISM is large enough. The thermal emission of the dust in the density enhancement at the shock interface between the stellar wind and the the ISM can be detected in the far-IR (Ueta et al. 2006, 2009). While a detached shell produced by TPs would be spherical, in the case of wind-ISM interaction the shape of the shell will depend on the space motion of the star through the ISM. A wind-ISM shell can look spherical as seen for R Cas (Ueta et al. 2009) if most of the space motion of the star relative to the ISM is in the radial direction. For stars with a high space motion (relative to the ISM), the shape of the bow shock will be more parabolic with the apex of the parabola in the direction of the star's motion relative to the ISM. In the case of CW Leo, the shape of the extended emission and the position of the star suggest that the stellar wind has driven a shock into the ISM. The far-IR emission is probably caused by the thermal emission of the piled-up dust at the shock interface.

One may think that the observed UV emission is produced by dust scattering of the interstellar light. However, the brightness ratio of FUV to NUV is ~ 10 (see Table 1), which is much higher than expected in that case (of the order of ~ 2.4 ; SC). The only other AGB star with UV data probing a wind-ISM interaction is Mira (Martin et al. 2007). Martin et al. suggest that collisional excitation of cool H₂ by hot electrons from the post-shock gas is responsible for the UV emission. The faint NUV emission can be explained by the H₂ emitting in the FUV band. SC suggest that the same mechanism may also be the dominant contributor to the FUV ring emission in CW Leo. The dust and the FUV emission have a similar spatial scale. For the planetary nebula NGC 6720, we note that van Hoof et al. (2010) find on the basis of PACS and SPIRE data that dust and H₂ are co-spatial and argue that H₂ has been formed on grain surfaces.

The structure seen in our data may also be the result of both mechanisms i.e., mass-loss variation and wind-ISM interaction. By estimating the interpulse period for CW Leo, we can check

whether the dust shell we see is from an earlier TP that is now interacting with the ISM.

Guelin et al. (1995) constrained the initial mass of CW Leo to be $3 \lesssim M \lesssim 5 M_{\odot}$ based on the isotopic ratios of ^{24,25,26}Mg. From the initial-final mass relation from Salaris et al. (2009), this implies a likely final mass (and essentially the current core mass) of 0.7–0.9 M_⊙. From the core mass interpulse period relation of Wagenhuber & Groenewegen (1998) for solar metallicity stars, this implies an interpulse period of 6 000–33 000 years.

Scaling the mass loss and the wind velocity in SC with our assumed values, the flow timescale in the unshocked and shocked winds is 19 900 and 56 000 yr (very long because of the very low velocity of 1.2 km s⁻¹ in this region, see SC for details), for a total lower limit to the duration of the mass-loss phase of about 75 000 years. If TPs were to modulate the mass loss, as hypothesised for the origin for the detached shells discussed earlier, one could expect at least one other TP to have occurred during the time it took the envelope to expand this far. No obvious density enhancement is evident in the unshocked wind in the PACS and SPIRE images, which suggests that the interpulse period is at least 19 000 years. However, the dynamical and interpulse timescales are compatible, so it is possible that the bow shock and dust emission are not only the result of a steady outflow interacting with the ISM, but might include the effect of an enhanced wind of short duration due to a recent TP (or pulses).

Table 1. Derived fluxes for the extended emission

λ (μm)	Flux (Jy)	λ (μm)	Flux (Jy)	λ (μm)	Flux (Jy)
0.15	$(20 \pm 0.2) \times 10^{-4}$	70	3.51 ± 0.54	250	4.31 ± 0.66
0.23	$(2 \pm 0.2) \times 10^{-4}$	160	7.70 ± 1.17	350	1.70 ± 0.27
				550	0.73 ± 0.14

4.2. Space motion of the star and the ISM flow velocity

From the adopted radial velocity, distance, and proper motion, the heliocentric space velocity of the star is derived to be about 25.1 km s⁻¹ at a heliocentric inclination angle of the space motion vector of 47.8 degrees (measured from the plane of the sky, away from us) and a PA of 81.3° for the proper-motion vector in the plane of the sky.

In the PACS/SPIRE wavebands, the observed far-IR surface brightness is expected to be proportional to the column density of the dusty material in the shell because the optical depth of the shell is much lower than unity. Because the bow shock interface is a parabolic surface arbitrarily oriented in space, the column density tends to reach its highest value where the bow shock cone intersects with the plane of the sky including the central star. Thus, the apparent shape of the bow shock is the conic section of the bow shock. Therefore, given the analytical formula of the bow shock structure (Wilkin 1996), we can fit the observed surface brightness of the bow shock to the conic section of the bow shock cone to derive the heliocentric orientation of the bow shock (e.g. Ueta et al. 2008; 2009). From this fitting, we determined that the apex of the bow shock cone is oriented at $61^{\circ}9 \pm 0^{\circ}3$ (this is degenerate, in a sense that it could be pointing away from us or towards us) with respect to the plane of the sky into the PA of 88° with the deprojected stand-off distance of $(8.0 \pm 0.3) \times 10^{17}$ cm.

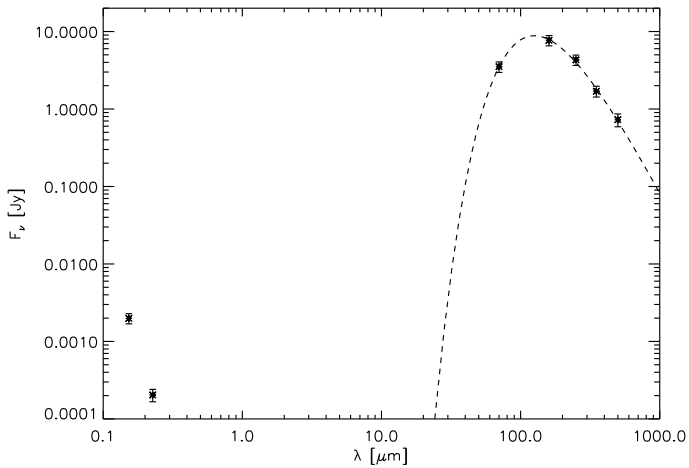


Fig. 3. Modified black body ($T = 25 \pm 3$ K and $\beta = 1.6 \pm 0.4$) fit (dashed curve) to the derived fluxes (symbols) for the extended emission.

Using these numbers in the ram pressure balance equation $V_\star = \sqrt{\frac{\dot{M} V_{\text{exp}}}{4\pi \mu_{\text{H}} m_{\text{H}} n_{\text{ISM}} R_0^2}}$ for a mean nucleus number per hydrogen nucleus of $\mu_{\text{H}} = 1.4$, the relative velocity of the star with respect to the ISM is $V_\star = (106.6 \pm 8.7) / \sqrt{n_{\text{ISM}}}$ km s⁻¹, where n_{ISM} is the number density of the ISM local to CW Leo in cm⁻³.

By following the scheme of Johnson & Soderblom (1987, also see Ueta et al. 2008), the heliocentric space velocity components of the star can be converted to the heliocentric Galactic space velocity components [U, V, W] of [21.6 ± 3.9, 12.6 ± 3.5, -1.8 ± 3.3] km s⁻¹, and also to the LSR Galactic space velocity components of [30.6 ± 3.9, 24.6 ± 3.5, 5.2 ± 3.3] km s⁻¹. The heliocentric ISM flow velocity is 117.6 km s⁻¹ if the bow cone is facing us (i.e. the apex pointing toward) or 82.6 km s⁻¹ if the bow cone is facing away from us.

Wareing et al. successfully modelled bow shocks for AGB stars using 3-D hydrodynamical models (RHya and Mira in Wareing et al. 2006, 2007a). Their models were able to reproduce in great detail all the components of a bow shock (astropause, astrotail, vortices) and constrain the space velocity of the star, the ISM density, and the mass-loss rate. The models were built by varying the velocity of the star relative to the ISM, the ISM density and the mass loss rate and the effect of those physical parameters on the shape of the bow shock can be seen in Wareing et al. (2007b). From the Wareing models, we can see that for ISM densities ≤ 2 cm⁻³ (which implies $V_\star \geq 75$ km s⁻¹) and after an evolution of 50 000 yr into the AGB phase, the bow shock does not resemble our data. The models have a more flattened bow shock with the star closer to the apex of the shock. This is for a mass-loss rate between $5 \times 10^{-7} M_\odot \text{ yr}^{-1}$ and $10^{-6} M_\odot \text{ yr}^{-1}$, which is an order of magnitude lower than the value assumed for CW Leo. For a higher mass-loss rate, we would expect an even more important departure from sphericity with a significant tail of ejecta. This suggests that the density of the local ISM to CW Leo is probably higher than 2 cm⁻³ implying an upper limit of 75 km s⁻¹ to V_\star , the stellar velocity relative to the ISM.

Acknowledgements. D.L, M.G, J.B, W.D, K.E, R.H, C.J, S.R, P.R and B.V acknowledge support from the Belgian Federal Science Policy Office via the PRODEX Programme of ESA. PACS has been developed by a consortium of institutes led by MPE (Germany) and including UVIE (Austria); KUL, CSL,

IMEC (Belgium); CEA, LAM (France); MPA (Germany); IFSI, OAP/AOT, OAA/CAISMI, LENS, SISSA (Italy); IAC (Spain). This development has been supported by the funding agencies BMVIT (Austria), ESA-PRODEX (Belgium), CEA/CNES (France), DLR (Germany), ASI (Italy), and CICT/MCT (Spain). SPIRE has been developed by a consortium of institutes led by Cardiff Univ. (UK) and including Univ. Lethbridge (Canada); NAOC (China); CEA, LAM (France); IFSI, Univ. Padua (Italy); IAC (Spain); Stockholm Observatory (Sweden); Imperial College London, RAL, UCL-MSSL, UKATC, Univ. Sussex (UK); and Caltech, JPL, NHSC, Univ. Colorado (USA). This development has been supported by national funding agencies: CSA (Canada); NAOC (China); CEA, CNES, CNRS (France); ASI (Italy); MCINN (Spain); SNSB (Sweden); STFC (UK); and NASA (USA) Data presented in this paper were analysed using “HIPE”, a joint development by the Herschel Science Ground Segment Consortium, consisting of ESA, the NASA Herschel Science Center, and the HIFI, PACS and SPIRE consortia. FK acknowledges funding by the Austrian Science Fund FWF under project numbers P18939-N16 and I163-N16.

References

- Becklin, E.E., Frogel, J.A., Hyland, A.R., Kristian, J., Neugebauer, G. 1969, ApJ, 158, L133
- Griffin, M.J., Abergel, A., Ade, P.A.R., et al. 2010, A&A this issue
- Fong, D., Meixner, M., Shah, R.Y. 2003, ApJ, 582, L39
- Groenewegen, M.A.T., van der Veen, W.E.C.J. & Matthews, H.E. 1998, A&A, 339, 489
- Groenewegen, M.A.T., Sevenster, M., Spoon, H.W.W., & Perez I. 2002, A&A, 390, 501
- Guelin, M., Forestini, M., Valiron, P., et al. 1995, A&A, 297, 183
- Johnson, D. R. H., & Soderblom, D. R. 1987, AJ, 93, 864
- Kerschbaum, F., Ladjal, D., Ottensamer, R., et al. 2010, A&A, this issue
- Leão, I.C., de Laverny, P., Mékarnia, D., de Medeiros, J.R., & Vandame, B. 2006, A&A, 455, 187
- Martin, D.C., Fanson, J., Schiminovich, D., et al. 2005, ApJ, 619, L1
- Martin, D.C., Seibert, M., Neill, J.D., et al. 2007, Nature, 448, 780
- Mauron, N., & Huggins, P.J. 1999, A&A, 349, 203
- Mauron, N., & Huggins, P.J. 2000, A&A, 359, 707
- Mauron, N., de Laverny, P., & Lopez, B. 2003, A&A, 401, 985
- Menten, K.M., Reid, M.J., Krügel, E., Claussen, M.J. & Sahai, R. 2006, A&A, 453, 301
- Olofsson, H., Carlström, U., Eriksson, K., et al. 1990, A&A, 230, L13
- Pilbratt, G., et al. 2010, A&A this issue
- Poglitsch, A., Waelkens, C., Geis, N., et al. 2010, A&A this issue
- Rouleau, F., & Martin, P.G., 1991, ApJ, 377, 526
- Sahai, R., & Chronopoulos, C.K. 2010, ApJ, 711, L53
- Salaris, M., Serenelli, A., Weiss, A., Miller Bertolami, M. 2009, ApJ, 692, 1013
- Swinyard, B.M., Ade, P.A.R., Baluteau, J.-P., et al. 2010, A&A this issue
- Ueta, T., Izumiura, H., Yamamura, I., et al. 2008, PASJ, 60, S407
- Ueta, T., Hideyuki, I., Yamamura, I., et al. 2009, arXiv0905.0756
- Ueta, T., Speck, A.K., Stencel, R.E. et al. 2006, ApJ, 648, L39
- van Hoof, P.A.M., Barlow, M.J., Van de Steene, G.C., et al. 2010, A&A this issue
- Volk, K., & Kwok, S. 1988, ApJ, 331, 435
- Wagenhuber, J. & Groenewegen, M.A.T. 1998, A&A, 340, 183
- Wareing, C.J., Zijlstra, A.A., Speck, A.K. et al. 2006, MNRAS, 372, L63
- Wareing, C.J., Zijlstra, A.A., & O’Brien, T.J. 2007b, MNRAS, 382, 1233
- Wareing, C.J., Zijlstra, A.A., & O’Brien, T.J., & Seibert, M. 2007a, ApJ, 670, L125
- Wilkin, F. P. 1996, ApJ, 459, L31
- Young, K., Phillips, T.G., Knapp, G.R. 1993, ApJ, 409, 725
- Zijlstra, A.A., Loup, C., Waters, L.B.F.M., de Jong, T. 1992, A&A, 265, L5

¹ Instituut voor Sterrenkunde, Katholieke Universiteit Leuven, Celestijnenlaan 200D, B-3001 Leuven, Belgium e-mail: Djazia.Ladjal@ster.kuleuven.be

² Department of Physics and Astronomy, University College London, Gower Street, London WC1E 6BT

³ Koninklijke Sterrenwacht van België, Ringlaan 3, B-1180 Brussels, Belgium

⁴ Dept. of Physics and Astronomy, University of Denver, Mail Stop 6900, Denver, CO 80208, USA

⁵ Radio Astronomy Laboratory, University of California at Berkeley, CA 94720, USA

⁶ Sterrenkundig Instituut Anton Pannekoek, Universiteit van Amsterdam, Kruislaan 403, NL-1098 Amsterdam, The Netherlands

⁷ School of Physics and Astronomy, Cardiff University, 5 The Parade, Cardiff, Wales CF24 3YB, UK

⁸ UK Astronomy Technology Centre, Royal Observatory Edinburgh,
Blackford Hill, Edinburgh EH9 3HJ, UK

⁹ University Vienna, Department of Astronomy, Türkenschanzstrasse
17, A-1180 Wien, Austria

¹⁰ Space Science and Technology Department, Rutherford Appleton
Laboratory, Oxfordshire, OX11 0QX, UK

¹¹ Dept of Astronomy, Stockholm University, AlbaNova University
Center, Roslagstullsbacken 21, 10691 Stockholm, Sweden

¹² Department of Physics, University of Lethbridge, Alberta, Canada